Thermo-osmotic slip flows around a thermophoretic microparticle characterized by optical trapping of tracers

Tetsuro Tsuji◉,[*] Satoshi Mei, and Satoshi Taguchi◉
Graduate School of Informatics, Kyoto University, Kyoto 606-8501, Japan

Thermo-osmotic flow around a microparticle in a liquid is characterized by observing and analyzing the distribution of tiny particles, i.e., tracers, near the surface of the microparticle. First, an optical-trapping laser is used to localize the tracer motion along a circular path near the circumference of the microparticle. Then, upon creating an overall temperature gradient in the liquid, the tracers on the circular path, originally uniformly distributed, gather toward the hotter side of the microparticle, indicating a flow along the particle toward the heat. Analyzing the tracer distribution further, it is found that (i) the flow magnitude decreases with the distance from the surface and (ii) changing the surface property of the microparticle results in a change in the flow magnitude. These results show that the observed flow is a thermally induced slip flow along the surface of the microparticle. Then, assuming a simple slip boundary condition for a fluid equation, we evaluate the magnitude of the slip coefficient based on two kinds of experimental data: (i) the thermophoretic velocity of the microparticle and (ii) the thermo-osmotic flow around the microparticle. The results of the two approaches are in quantitative agreement. They are also compared with those of theoretical models for a slip flow in existing studies.

I. INTRODUCTION

When a fluid is in contact with a solid surface with an inhomogeneous temperature distribution, thermally induced slip flows manifest. These flows are often called thermo-osmosis or thermo-osmotic flows in the literature [1–5] and are considered novel tools for microscale and/or nanoscale material transport [6–8] and manipulation [9, 10]. Thermo-osmosis has multiple physical origins, such as an excess enthalpy variation [11,12] and thermoelectric [13–15] and Marangoni effects [16–18].

A growing interest in thermo-osmosis originates from the recent developments on photothermal effects and thermoplasmonics [19–21], where fluids and/or solid surfaces can be heated locally on the nanoscale. These localized heat sources lead to a steep temperature gradient, inducing thermo-osmotic flows of the detectable order of magnitude, e.g., a few tens of μm s^{-1} [10]. Nonetheless, due to the multiphysics nature and difficulties in experimental evaluation, comparisons between theory and experiment are considered challenging. To tackle this situation, the present paper develops a tool for the experimental evaluation of thermo-osmotic slip flows and applies it to the characterization of the flows around microparticles.

Before describing the developed tools, let us explain why we are interested in the flows around particles. Thermo-osmosis around particles is particularly important among its applications, because it is one of the driving mechanisms of thermophoresis of tiny particles [22–25] and active matter [26–29]. Thermophoresis has been widely explored for separating a mixture [30–33], characterization in bioscience [34–36], and optothermal manipulation of nanomaterial [37,38] and biomaterial [39]. Nevertheless, the profiles of thermo-osmotic flows around thermophoretic particles have not been evaluated and, thus, the contribution of the flow to thermophoresis remains unclear. The motivation of the present paper is to present the direct connection between the thermophoresis of a particle and the thermally induced flow around it. In Refs. [40] and [26], the thermally induced slip flows around a micro- and Janus particle, respectively, have been observed but the flow profile was not quantified. Thermo-osmotic flows on the flat surface have been observed in Refs. [1,10] and that around a Janus particle in Ref. [41]. However, because the thermally induced flows occur near the surface, tracers for flow visualization were scarce, preventing a systematic flow characterization.

We now explain the tool proposed in this paper. To overcome the experimental difficulty above, we use optical

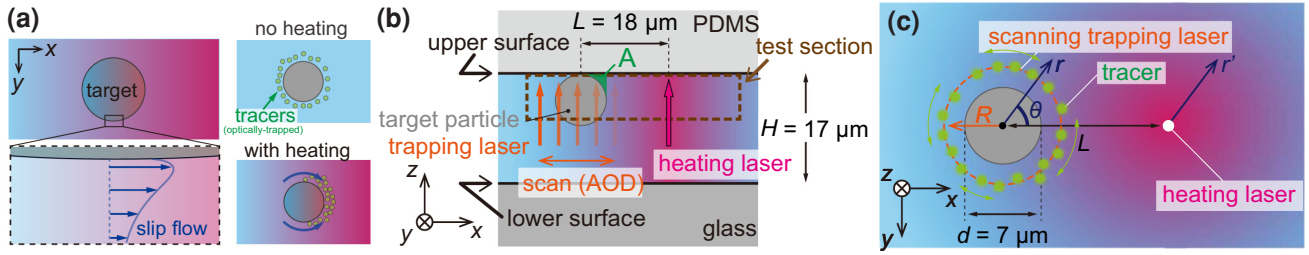---

[*]tsuji.tetsuro.7x@kyoto-u.ac.jp

FIG. 1. (a) The concept of the proposed method to investigate a thermally induced flow around a target microparticle, which is immersed in a nonuniformly heated fluid. Tracers are optically trapped around the microparticle and play the role of flow detectors when the surrounding fluid is heated. (b),(c) Schematics of the experiments. In the experiment, the target microparticle is placed in a microchannel. (b) A side view. The microchannel consists of the upper surface, made of polydimethylsiloxane (PDMS), and the lower surface, made of a glass substrate. The target particle, with a diameter of 7 μm, is immobilized on the upper surface of the microchannel with a height of 17 μm. A heating laser is irradiated at $L = 18$ μm horizontally away from the center of the target. (c) The bottom view (i.e., the camera view) of a test section. A scanning trapping laser on a circular path with a radius of R confines fluorescent tracers in the vicinity of the target microparticle.

trapping (or an optical tweezer) [42,43]. In recent years, optical trapping has become a powerful tool for the control of tiny objects [44,45]. Here, using the optical tweezer, we trap tracers as flow detectors [see the concept of the present paper, shown in Fig. 1(a)]. By confining the tracers optically in a test section, which is a circular path around a target microparticle, we facilitate the visualization of thermally induced flows near the particle surface, which is immersed in a water solution. In particular, we focus on the spatial dependence of the flow, the surface characteristics of the microparticle, and the connection between thermo-osmosis and thermophoresis.

II. EXPERIMENTAL METHOD

We will briefly explain the present experimental method, leaving full details in Appendix A. A target polystyrene particle with a diameter of $d = 7$ μm is immobilized at the upper surface of a microchannel with a height of 17 μm, as shown in Fig. 1(b). The immobilization is necessary to focus on a flow around the target particle without its translocation.

Then, a focused trapping laser with a wavelength of 1064 nm is irradiated to the upper surface of the microchannel. The trapping laser is scanned circularly around the target particle so that polystyrene fluorescent tracers with a diameter of 500 nm are optically trapped around the target particle, as shown in Fig. 1(c). A scanning circular path has a radius R, which is an experimental parameter and is chosen as $R = 4.4, 5.4, 6.5,$ or 7.5 μm. We use a polar coordinate system with a radial position r and an angle θ measured from a line connecting the center of the target particle and a heating spot [Fig. 1(c)]. The optical trapping is loose on the circular path, on which the tracers undergo the Brownian motion in the θ direction [Fig. 1(c)].

After a while, many tracers are held on the circular path, so that the spatial distribution of the tracers becomes almost uniform with respect to θ, as shown in Fig. 1(a). Then, at time $t = 0$ s, a focused heating laser with a wavelength of 1480 nm and with a power P is irradiated to the upper surface of the microchannel at a position distant from the target particle [Figs. 1(b) and 1(c)]. The temperature gradient of the fluid is maintained by a photothermal conversion: the absorption of a near-infrared laser in water [46–49]. Such optical heating is necessary to achieve a steep temperature gradient for the generation of the thermo-osmotic flow with a detectable magnitude.

The distance between the target particle and the focus of the heating laser is set to $L = 18.0 \pm 0.1$ μm and the distance from the heating laser is denoted by r' [Fig. 1(c)]. The results of the temperature measurement for the heating-laser power of $P = 13.5, 30.2, 46.7,$ and 78.7 mW are summarized in Appendix B; the temperature difference across the particle is approximately 14 K at most and the magnitude of the temperature gradient is of the order of 1 K μm^{-1}. We observe the change in the tracer distribution on the circular path in the x-y plane [Fig. 1(c)] after the onset of laser heating.

III. MODEL

In this section, we present a simple model that describes the physical situation of the experiment. For simplicity, we consider the steady state, which is realized after a few tens of seconds of the heating-laser irradiation. In the experiment, the presence of the upper surface of the microchannel yields the three-dimensional flow field and temperature distribution. To simplify the analysis, however, we neglect the presence of the microchannel wall and consider the flow to be axisymmetric. This means that the tracer motion in our model can be represented by the motion in the equatorial x-y plane of the target particle.

Furthermore, in our model, we assume that the target particle is small enough and that the temperature variation far from the particle depends only on x (for a detailed discussion, see Appendix B).

A. Fluids

The temperature of the fluid and that inside the target particle are denoted by T_f and T_s, respectively. Since the thermal Péclet number Pe_T is small, i.e., $\mathrm{Pe}_T \ll 1$, we can neglect the convection term; the temperature fields T_f and T_s obey the steady heat-conduction equations. For instance, when the reference length is 10 μm, the reference speed is 1 μm, and the thermal diffusivity is 1.4×10^{-7} m^2 s^{-1}, we have $\mathrm{Pe}_T = 7 \times 10^{-5}$.

The condition for the temperature imposed at infinity is $T_f \to T_0 + \alpha x$ ($r \equiv |\mathbf{x}| \to \infty$), with a constant temperature gradient $\alpha (> 0)$. Note that the x direction corresponds to $\theta = 0$ in Fig. 1(c) and that T_0 is a reference temperature at the center of the target particle. At the surface of the target particle $r = a (= d/2)$, the temperature and the heat flux in the normal direction to the sphere surface are continuous. Then, we readily obtain

$$\frac{T_f - T_0}{\alpha a} = \left(1 + \frac{a^3}{r^3}\xi_f\right)\frac{r}{a}\cos\theta, \quad \xi_f \equiv \frac{\kappa_f - \kappa_s}{2\kappa_f + \kappa_s}, \quad (1a)$$

$$\frac{T_s - T_0}{\alpha a} = \xi_s \frac{r}{a}\cos\theta, \quad \xi_s \equiv \frac{3\kappa_f}{2\kappa_f + \kappa_s}(= \xi_f + 1), \quad (1b)$$

where αa is a characteristic temperature difference over a distance a, κ_f and κ_s are the thermal conductivities of the fluid and the target particle, respectively, and ξ_f and ξ_s are nondimensional parameters related to the thermal conductivity. In this paper, the temperature dependence of thermal conductivity is not considered, i.e., the constants $\kappa_f = 0.6$ W m^{-1} K^{-1}, $\kappa_s = 0.2$ W m^{-1} K^{-1}, $\xi_f \approx 0.286$, and $\xi_s \approx 1.286$ are used.

The temperature field in Eq. (1) induces a fluid flow through a slip boundary condition, i.e., on the sphere surface the flow velocity vector $\mathbf{u}$ satisfies

$$\begin{aligned} u_r &\equiv \mathbf{u} \cdot \mathbf{e}_r = 0, \\ u_\theta &\equiv \mathbf{u} \cdot \mathbf{e}_\theta = -K\mathbf{e}_\theta \cdot \nabla T_f, \end{aligned} \quad (r = a), \quad (2)$$

where $\mathbf{e}_r$ and $\mathbf{e}_\theta$ are the unit vectors in the r and θ directions, respectively, and K is a thermo-osmotic slip coefficient; an alternative definition, $\chi = -KT_f|_{r=a}$, has also been used in the literature [1,10–12]. Here, the temperature gradients of both regions are equal: $\mathbf{e}_\theta \cdot \nabla T_f = \mathbf{e}_\theta \cdot \nabla T_s$ at $r = a$.

Note that Eq. (2) is different from the so-called Navier-slip condition, in which the slip velocity is related to the shear stress on the surface. Here, in Eq. (2), the slip velocity is related to the temperature gradient along the surface. Indeed, Eq. (2) is motivated by the thermal-slip condition

for a rarefied gas, which describes the creeping motion of a gas along a nonuniformly heated wall. For a rarefied gas, the slip conditions (i.e., the thermal-slip and Navier-type shear-slip conditions) can be derived systematically through an analysis of the Boltzmann equation and its boundary condition (see, e.g., Ref. [50] and references therein). In the case of a liquid flow, unfortunately, there is no such theory and the thermal slip in Eq. (2) should be taken as being phenomenological. We need further theoretical work to determine the numerical value of the slip coefficient.

Assuming that the Reynolds number Re is small, i.e., $\mathrm{Re} \ll 1$ (e.g., a kinematic viscosity of approximately 10^{-6} m^2 s^{-1} leads to $\mathrm{Re} \sim 10^{-5}$), the flow field $\mathbf{u}$ satisfies the Stokes equation, which can be solved explicitly under the boundary condition given in Eq. (2) and the condition imposed at infinity, namely, $\mathbf{u} = 0$ at $r \to \infty$. The results are

$$\frac{u_r}{\alpha K} = \xi_s \left(-1 + \frac{a^2}{r^2}\right)\frac{a}{r}\cos\theta, \quad (3a)$$

$$\frac{u_\theta}{\alpha K} = \xi_s \left(1 + \frac{a^2}{r^2}\right)\frac{a}{2r}\sin\theta, \quad (3b)$$

$$\frac{p}{\alpha K(\eta/a)} = -\xi_s \frac{a^2}{r^2}\cos\theta, \quad (3c)$$

where p is the pressure, αK is the product of the temperature gradient and the slip coefficient, namely, the characteristic speed of thermally induced flow, and η is the viscosity of the fluid. In particular, on the sphere surface, we have

$$u_\theta = -u_s \sin\theta, \quad u_s \equiv -\xi_s K\alpha \quad (r = a), \quad (4)$$

where the sign of u_s is chosen so that u_s is positive when the slip flow is induced in the negative θ direction, i.e., toward the hotter side of the target particle. When the thermal conductivity satisfies $\kappa_s = \kappa_f$, it leads to $\xi_s = 1$ and thus $u_s = -K\alpha$. On the other hand, when the thermal conductivity of the target is huge, e.g., in the case of a metal particle, we have $\kappa_s \gg \kappa_f$ that yields $\xi_s \ll 1$, resulting in no slip flows on the sphere surface.

B. Target particle

The fluid force F_i ($i = x, y, z$) acting on the target particle is obtained from the surface integral $F_i = \int p_{ij} n_j \, dS$, where p_{ij} denotes the stress tensor for a Newtonian fluid, n_i is a unit vector on the surface pointing to the fluid, dS is an area element, and the integral is carried out over the sphere surface $r = a$. The x component F_x is then readily obtained as $F_x = 4\pi a\eta\xi_s K\alpha$ using Eq. (3). Therefore, in this model, the x component of the thermophoretic velocity of the target particle, v_T^{target}, is computed from the balance between the force F_x and the Stokes drag $6\pi a\eta v_T^{\mathrm{target}}$,

i.e., $v_T^{\text{target}} = (2/3)\xi_s K\alpha \, [= -(2/3)u_s]$. This means that the positive u_s (i.e., a slip flow toward the heat) induces the motion of the target particle toward the cold, $v_T^{\text{target}} < 0$.

Recall that, in general, the thermophoretic velocity $\mathbf{v}_T$ of particles is given by $\mathbf{v}_T = -D_T \nabla T_f$ phenomenologically, where D_T is called a thermophoretic mobility [22,23]. In this equation, the term ∇T_f should be understood as the temperature gradient at infinity; i.e., the effect of temperature deformation due to the presence of the target particle is confined in the mobility D_T. Therefore, by noting that $v_T^{\text{target}} = \mathbf{e}_x \cdot \mathbf{v}_T$ and $\mathbf{e}_x \cdot \nabla T_f = \alpha$, where $\mathbf{e}_x$ is a unit vector in the x direction, the thermophoretic mobility of the target, D_T^{target}, is obtained as

$$D_T^{\text{target}} \equiv -\frac{v_T^{\text{target}}}{\alpha} = -\frac{2}{3}\xi_s K, \qquad (5)$$

which is the relation between D_T^{target} and the slip coefficient K. Experimentally, the slip coefficient K can be estimated from Eq. (5) through the evaluation of D_T^{target}, i.e., v_T^{target} and α.

C. Tracers

Now, suppose that the tracers are confined in the circular path $r = R$ because of the trapping laser [see Fig. 1(c)]. The number density of the tracers is denoted by c. The velocity of the tracer, $\mathbf{v}$, is the sum of the flow velocity $\mathbf{u}$ and the thermophoretic velocity $\mathbf{v}_T^{\text{tracer}} \equiv -D_T^{\text{tracer}} \nabla T_f$, where D_T^{tracer} is the thermophoretic mobility of the tracer. In this equation, ∇T_f should be interpreted as a local quantity due to the smallness of the tracer, i.e., ∇T_f is computed from Eq. (1a). Then, the tracer distribution c satisfies a steady drift-diffusion equation with a drift velocity $\mathbf{v} \equiv \mathbf{u} + \mathbf{v}_T^{\text{tracer}}$. The θ component of $\mathbf{v}$ can be computed explicitly as $\mathbf{v} \cdot \mathbf{e}_\theta = -v^* \sin\theta$, where v^* is the flow magnitude in the direction toward the hotter region, i.e.,

$$v^* = -\xi_s \left(1 + \frac{a^2}{r^2}\right)\frac{a}{2r}\alpha K - \left(1 + \frac{a^3}{r^3}\xi_f\right)\alpha D_T^{\text{tracer}}. \quad (6)$$

Because of the scanning trapping laser at $r = R$, we assume that the radial motion of the tracer is suppressed and that only the motion in the θ direction is significant. Further assuming that there is no steady flux of the tracers, the drift-diffusion equation is reduced to the balance between the drift and diffusion in the θ direction at $r = R$:

$$c(\mathbf{v} \cdot \mathbf{e}_\theta) - \frac{D}{R}\frac{\partial c}{\partial \theta} = 0, \qquad (7)$$

where D is the diffusion coefficient of the trapped tracers. Equation (7) can be solved explicitly as

$$\frac{c}{c_0} = \exp(\gamma \cos\theta), \qquad (8a)$$

$$\gamma \equiv \frac{v^*|_{r=R}}{D/R}, \qquad (8b)$$

where c_0 is a normalization constant and the prefactor γ in Eq. (8b) is the ratio between the magnitude of the drift velocity v^* and the diffusive speed D/R. Note that γ depends on the radius of the circular path R, the thermophoretic mobility D_T^{target} (or K) and D_T^{tracer}, and the temperature gradient α. When $\gamma > 0$ (or $\gamma < 0$), the number density of the tracers c takes a maximum at $\theta = 0$ (or π), i.e., the hotter (or colder) side of the target particle. When $|\gamma| \approx 0$, the diffusion dominates and c tends to be distributed uniformly on the circular path.

The model given in Eq. (8) is used to fit and analyze the experimental results. The adequateness of Eq. (8) is investigated in Appendix C. The technical details of the fitting procedure are given in Appendix D. Once γ, D_T^{tracer}, and α have been experimentally obtained, the slip coefficient K can be evaluated using Eqs. (6) and (8b). Later, we will compare K thus obtained with that estimated in the method described previously in Sec. III B.

IV. RESULTS AND DISCUSSION

A. Control experiments

Before setting out the experimental results in detail, we show the outcome of some control experiments.

1. Thermophoresis of the tracers

First, we observe the thermophoretic motion of tracers in the absence of the target particle. In the previous studies, the tracers are known to move against the temperature gradient with the present experimental condition [32,51]. That is, D_T^{tracer} is positive.

Figures 2(a)–2(e) show snapshots of the thermophoresis of tracers (white dots) near the upper surface of the microchannel at time $t = 0, 5, \ldots, 30$ s, where the heating laser with a power $P = 13.5$ mW is irradiated at the center of the images. We observe two characteristic features in the figure: (i) the fluorescent intensity increases near the radial distance $r' \approx 0$ μm, where r' is the distance from the heating laser; and (ii) the dark region with low intensity spreads over $r' \gtrsim 10$ μm.

Feature (i) is attributed to the tracers accumulated near the lower surface. Such an accumulation is due to thermophoresis in the negative z direction [52], which occurs due to a cooling at the lower glass substrate with a rather high thermal conductivity compared with water and/or the upper surface, made of polydimethylsiloxane (PDMS). These are beyond the scope of the present paper.

On the other hand, feature (ii) indicates the onset of the thermophoresis of tracers in the radial direction. Figure 2(f) shows the time development of the normalized intensity distribution in Figs. 2(a)–2(e), and the depletion of the tracer, i.e., positive D_T^{tracer}, is clearly presented.
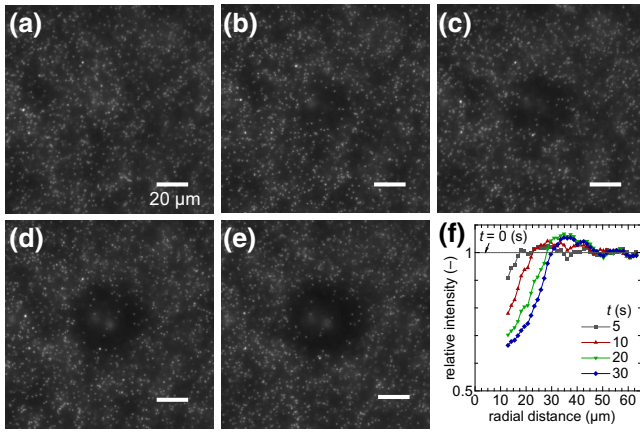
FIG. 2. The thermophoresis of the tracers. Snapshots at (a) $t = 0$, (b) 5, (c) 10, (d) 20, and (e) 30 s, where a heating laser with $P = 13.5$ mW is irradiated at the center of the images. (f) The relative-intensity distribution at $t = 5$, 10, 20, and 30 s averaged over 5 s as the function of the distance r' from the laser.

2. Thermophoresis of the target particle

Figure 3 shows the thermophoresis of the target particle before immobilization. Here and in what follows, the target has carboxylate-surface modification unless otherwise stated. Note that a target, without immobilization, settles out onto the lower surface of the microchannel because of its large sedimentation velocity (> 1 µm s^{-1}).

As shown in Fig. 3(a), at $t = 0$ s, the target particle is placed at a distance $r' = 19.4$ µm away from the heating laser. As time goes on [see Figs. 3(b)–3(e)], the target particle is repelled from the heated spot, moving over
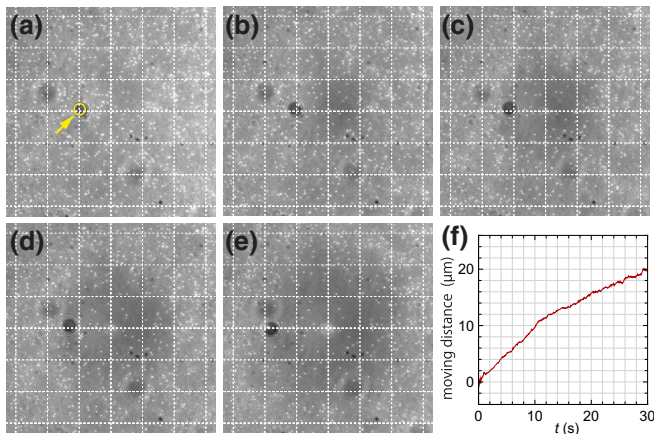

FIG. 3. Bright-field imaging of the thermophoresis of a target particle with a carboxylate-modified surface. Snapshots at (a) $t = 0$, (b) 1, (c) 3, (d) 7, and (e) 20 s, where a heating laser is irradiated at the center of the images. The target particle is indicated by an arrow and a yellow circle with a diameter of 7 µm in (a) as a guide to the eye. The grid spacing is 20 µm. (f) The moving distance as a function of time t.

almost 20 µm in a duration of 20 s. Figure 3(f) shows the moving distance of the target particle as a function of time, obtained using the particle-tracking analysis of the open-source ImageJ image-processing software package.

The average speed of the target particle up to $t = 2$ s is 0.89 µm s^{-1} and the average temperature and temperature gradient over the trajectory are 328 K and -1.77 ± 0.08 K µm^{-1}, respectively, leading to the thermophoretic mobility of the target, $D_T^{\text{target}} = 0.50 \pm 0.17$ µm^2 s^{-1} K^{-1}.

3. Thermophoresis of the trapped tracers

In this section, we show the tracer motion, which is trapped on the circular path in the absence of the target particle, as shown in Fig. 4(a). This is a control experiment to ensure that the irradiation of the scanning trapping laser does not affect the direction of thermophoresis of the tracers. The distance between the center of the scanning trapping laser and the heating laser is set to $L = 15.5$ µm and the laser power of the trapping laser is set to 71 mW.

Figures 4(b)–4(g) are time-averaged images of the tracer with the radius of the circular path $R = 4.4$ µm. For instance, Fig. 4(b) shows time-averaged images over -5 s $\leq t \leq 0$ s. Since these are time-averaged images, if a tracer does not look blurry, it is not a Brownian particle, i.e., the tracer is adhering to a channel wall [see, e.g., the tracers indicated by arrows in Fig. 4(e)].

It can be seen that the tracers near $\theta = 0$ are depleted as time goes on, i.e., the intensity reduces near $\theta = 0$. Moreover, the overall intensity decreases, indicating that some tracers escape from the optical trapping and move away from the hot region. Figure 4(h) shows the relative-intensity distribution near $r = R$ and $t = 15$ s [i.e., Fig. 4(e)] as a function of θ. The fitting is made by Eq. (8) with $\gamma = -0.52$ (see Appendix D), indicating the motion of tracers toward the colder side. In the absence of the
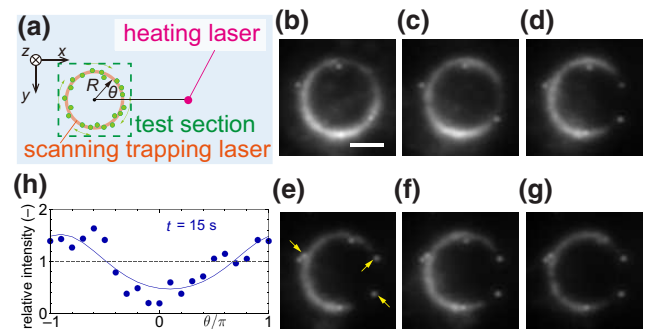

FIG. 4. (a) A schematic of an experiment in the absence of a target particle. (b)–(g) Time-averaged images over 5-s intervals: (b) $t = 0$, (c) 5, (d) 10, (e) 15, (f) 20, and (g) 25 s. The arrows in (e) indicate tracers stuck to the channel wall. These stuck tracers can become noise in the intensity analysis. Scale bar: 4 µm. (h) The relative-intensity profile at $r = R$ with respect to θ. The solid line indicates the fit given by Eq. (8).

target particle, the temperature gradient is uniform [see Eq. (1a)] and the slip flow is absent. Therefore, $|\gamma|$ corresponds to the phoretic Péclet number [53], i.e., the magnitude $|\gamma| \approx O(1)$ indicates that the thermophoresis of the tracers is competing with their diffusion. Noting that $\xi_f = 0$ (or $\kappa_f = \kappa_s$) and $K = 0$ without the target particle, the value of $\gamma = -0.52$ results in $D_T^{\mathrm{tracer}} = 0.10\ \mu\mathrm{m}^2\ \mathrm{s}^{-1}\ \mathrm{K}^{-1}$ using Eqs. (8b) and (6).

B. Observation of thermally induced flows

Let us describe the main results of the present paper, the thermally induced flow around the target particle. First, the results for a target particle with a carboxylate-modified surface are presented. The zeta potential ζ of the target particles is measured from the electrophoretic mobility (ELSZ-2000Z, Otsuka Electronics) as $\zeta = -46$ mV.

Figure 5(a) shows the schematic of the situation presented in Figs. 5(b)–5(f), which are the recorded images for various parameters $P = 78.7$, 46.7, and 30.2 mW (the power of the heating laser) and $R = 4.4$, 5.4, 6.5, and 7.5 μm (the radius of the scanning trapping laser); Video 1 shows the movie of Fig. 5(b). One can compare the effect of R by inspecting Figs. 5(b), 5(c), and 5(f) and that of P by inspecting Figs. 5(c), 5(d), and 5(e). Lowering the laser power to $P = 13.5$ mW does not reveal a significant change in the tracer distribution from the initial state.

First, it can be seen from Fig. 5(b) that the tracers, which are initially rather uniform in the θ variable, tend to gather toward the hotter side [i.e., the right-hand side; see Fig. 5(a)] as time goes on. This tendency is the same for other panels [see Figs. 5(c)–5(f)] and should be contrasted with Fig. 4 for a case without a target particle; the tracers gather toward the colder side.
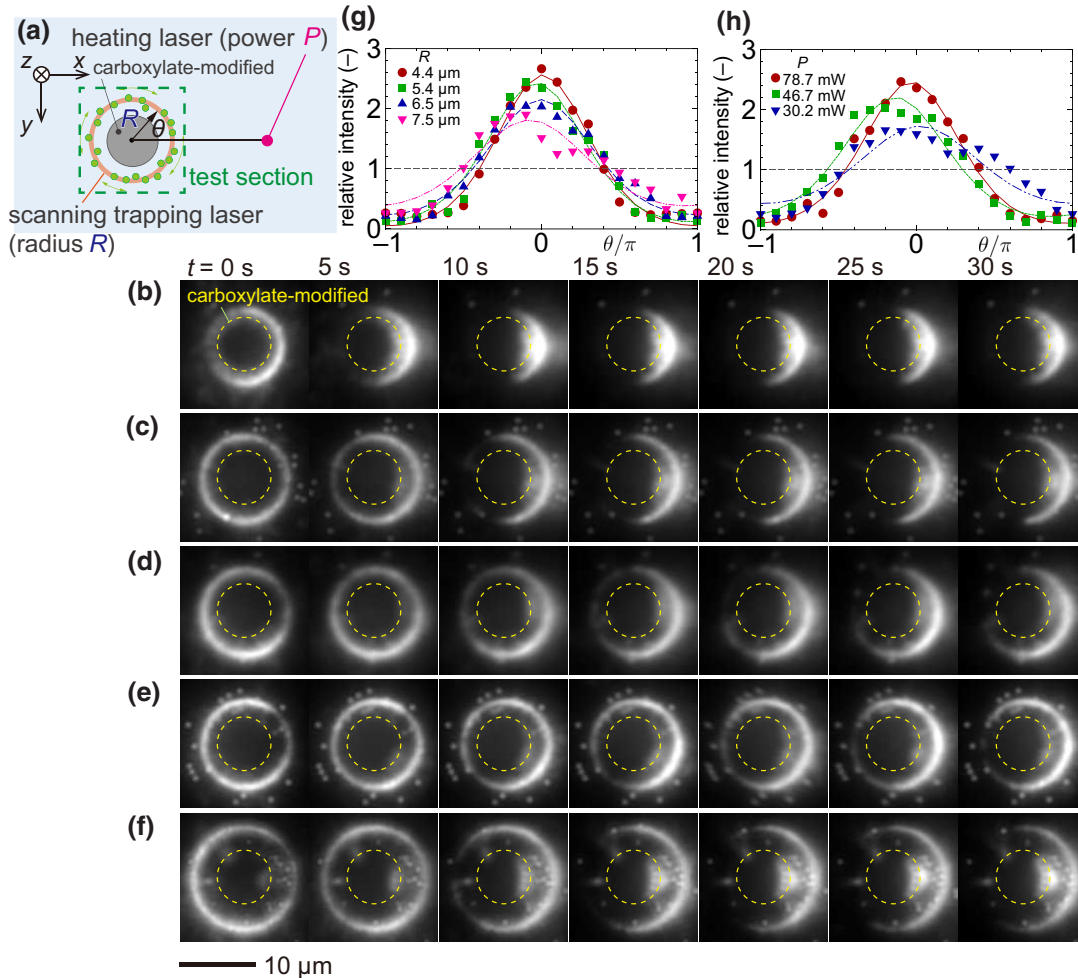

FIG. 5.　(a) A schematic of experiments in the presence of a target particle with a carboxylate-modified surface ($\zeta = -46.0$ mV). R is the radius of the scanning trapping laser and P is the power of the heating laser. (b)–(f) Time-averaged images over 5-s intervals for various values of P and R: (b),(c),(f) $P = 78.7$ mW, (d) $P = 46.7$ mW, and (e) $P = 30.2$ mW; (b) $R = 4.4\ \mu$m, (c)–(e) $R = 5.4\ \mu$m, and (f) $R = 6.5\ \mu$m. Since these are time-averaged images, if a tracer does not look blurry, it is adhering to the upper channel wall. (g),(h) Relative-intensity profiles as a function of θ; (g) $P = 78.7$ mW ($t = 25$ s) for various values of R and (h) $R = 5.4\ \mu$m for various values of P ($t = 30$ s). The lines in (g) and (h) indicate the fits given by Eq. (8). See also Video 1 for (b).
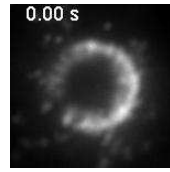
VIDEO 1. A video of Fig. 5(b): a target particle with a carboxylate-modified surface with $P = 78.7$ mW and $R = 4.4$ μm.

As can be seen from the comparison between Figs. 5(b) ($R = 4.4$ μm), 5(c) ($R = 5.4$ μm), and 5(f) ($R = 6.5$ μm), the movement of the tracers is more intense and faster for smaller R. To be more precise, at time $t = 5$ s, Fig. 5(b) starts to exhibit the depletion of the tracers near $\theta = \pi$ [the colder side; see Fig. 5(a)]; however, Figs. 5(c) and 5(f) show the apparent depletion near $\theta = \pi$ only for $t \geq 10$ s. At $t = 30$ s, where the distributions can be considered steady, the intensity near $\theta = 0$ seems to reach a maximum, indicating the accumulation near the hot side. To compare more quantitatively, we show in Fig. 5(g) the relative-intensity distribution (symbols) and the fitting using Eq. (8) (lines) (see also Appendix D). Although the results are qualitative, the plots in Fig. 5(g) capture the observations made in Figs. 5(b), 5(c), and 5(f).

It should be noted that some tracers seem trapped in the region between the upper wall of the microchannel and the target particle [see the region "A" in Fig. 1(b)], as clearly seen in Fig. 5(f) at $t \geq 10$ s. These tracers can stay there even when the scanning trapping laser is not irradiated. We suppose that the thermo-osmotic flow and the thermophoresis in the z direction may cause this trapping, but further discussion is difficult using only the present two-dimensional information on the x-y plane and thus is left for future work.

One can compare the effect of the heating-laser power P by examining Figs. 5(c) ($P = 78.7$ mW), 5(d) ($P = 46.7$ mW), and 5(e) ($P = 30.2$ mW). The corresponding temperature-gradient measurement given in Appendix B shows that $|\nabla T_f|$ is approximately 2.1 K μm^{-1} [Fig. 5(b)], 1.6 K μm^{-1} [Fig. 5(c)], and 1.0 K μm^{-1} [Fig. 5(d)], respectively, near $r' \approx L = 18$ μm, at which the target particle is fixed. Therefore, the tracer movement is more intense for the case with larger P. Figure 5(h) shows the corresponding relative-intensity distribution at $t = 30$ s. The sharper shape near $\theta = 0$ for larger P indicates the more intense accumulation of tracers near the hotter side.

Next, let us describe the thermally induced flow around a target particle with an amine-modified surface, the zeta potential ζ of which is measured as $\zeta = -23.7$ mV. The thermophoretic mobility of a target particle with an amine-modified surface is estimated in the same manner as in Sec. IV A 2 and we obtain $D_T^{\text{target}} = 0.29 \pm 0.08$ μm^2 s^{-1} K^{-1}, where the average temperature and temperature gradient are 320 K and -1.18 K μm^{-1},
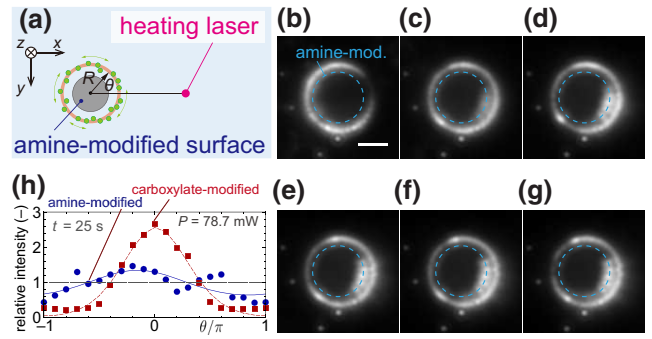

FIG. 6. (a) A schematic of experiments in the presence of a target particle with an amine-modified surface ($\zeta = -23.7$ mV). (b)–(g) Time-averaged images over 5-s intervals: (b) $t = 0$, (c) 5, (d) 10, (e) 15, (f) 20, and (g) 25 s. Scale bar: 4 μm. (h) The relative-intensity profile at $r = R$ with respect to θ for amine-modified surfaces (circle) and carboxylate-modified surfaces [square; see also Fig. 5(b) for microscope images]. The lines in (h) indicate the fits given by Eq. (8). See also Video 2 for (b)–(g).

respectively. This value of D_T^{target} is smaller than that of a target particle with a carboxylate-modified surface (see Sec. IV A 2).

Figure 6(a) shows the schematic of the situation presented in Figs. 6(b)–6(g), which are recorded images for $P = 78.7$ mW and $R = 4.4$ μm with a target particle with an amine-modified surface; Video 2 shows the movie of Figs. 6(b)–6(g). For a comparison with the case of a carboxylate-modified surface, see Fig. 5(b). Remarkably, the case of the amine-modified target results in a faint accumulation of tracers. As shown in Figs. 6(b)–6(g), the tracers gather slightly toward the hotter side but the accumulation is very weak compared with Fig. 5(b) for a carboxylate-modified target. This observation is further verified by the profile of the relative-intensity distribution, shown in Fig. 6(h) for both amine- (circle) and carboxylate- (square) modified surfaces. Since the surface modification is the only difference between these two cases, Fig. 6(h) is clear evidence that the observed tracer movement originates from surface phenomena.

C. Discussion

To compare the experimental results with existing models of thermally induced slip flows, we use the model
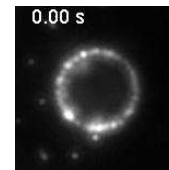
VIDEO 2. A video of Figs. 6(b)–6(g): a target particle with an amine-modified surface with $P = 78.7$ mW and $R = 4.4$ μm.

proposed in Ref. [13], in which a thin electric double-layer (EDL) approximation for a charged surface of a spherical colloid is applied under the Debye-Hückel approximation. The resulting slip velocity is written as

$$v_B = -v_0 \sin\theta \quad (r = a), \qquad (9a)$$

$$v_0 \equiv \frac{\varepsilon\psi_0^2}{8\eta}\left(1 - \frac{d\ln\varepsilon}{d\ln T_f}\right)\xi_s\frac{|\nabla T_f|_\infty}{T_f}, \qquad (9b)$$

where $|\nabla T_f|_\infty(=\alpha)$ is the temperature gradient at infinity, ε is the temperature-dependent electric permittivity, and ψ_0 is the electrostatic potential at the surface. We assume that $\psi_0 \approx \zeta$. The temperature dependence of ε for water is modeled as $\varepsilon/\varepsilon_0 = 305.7 \times \exp(-T_f/217)$ [54], where $\varepsilon_0 = 8.85 \times 10^{-12}$ F m^{-1} is the electric permittivity in vacuum. Furthermore, the empirical model of viscosity $\eta = (2.761 \times 10^{-6}) \times \exp(1713/T_f)$ Pa s [55] is used. For the above model, the slip coefficient K in Eq. (4) is expressed as $K = -v_0/(\xi_s\alpha)$ because $u_s = v_0$. To be more specific, we have

$$K = -\frac{\varepsilon\zeta^2}{8\eta T_f}\left(1 - \frac{d\ln\varepsilon}{d\ln T_f}\right). \qquad (10)$$

In Ref. [1], a similar form is proposed based on Derjaguin's model [56], with an enthalpy excess given by the EDL enthalpy with the Debye-Hückel approximation. This model was considered to analyze the thermo-osmosis on a bare glass substrate. The result was

$$K = -\frac{\chi}{T_f} = -\frac{\varepsilon\zeta^2}{8\eta T_f}. \qquad (11)$$

The theoretical prediction K obtained by Eqs. (10) and (11) can be compared with K obtained from the experiments via two possible methods:

(1) First, K can be obtained from the thermophoretic motion of the target, given in Eq. (5), because we have obtained D_T^{target} experimentally by particle tracking (see Sec. IV A 2).

(2) Second, K can be obtained from the observation of slip flows in Sec. IV B, namely, the tracer accumulation behavior given in Eq. (8), through the fitting of the value γ (for the results of fitting, see Figs. 5 and 6). Then, Eq. (6)
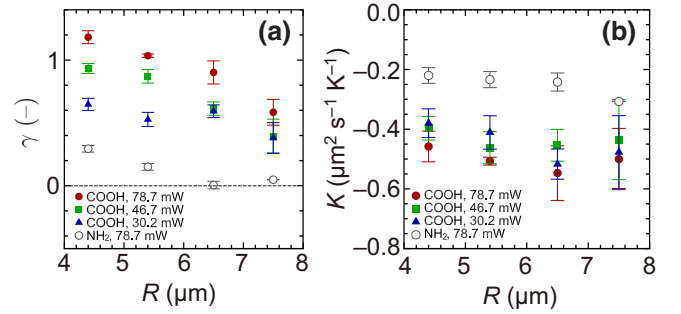

FIG. 7. (a) The values of γ as a function of the scanning radius R for carboxylate-modified (COOH, filled symbols) and amine-modified (NH$_2$, empty symbols) surfaces with heating power $P = 78.7$ (circle), 46.7 (square), and 30.2 mW (triangle). (b) The slip coefficient K computed from γ in (a) through Eqs. (8b) and (6).

and γ yield K, since we have already evaluated D_T^{tracer} in Sec. IV A 1.

Before going into the comparison between the theoretical prediction [Eqs. (10) and (11)] and the experimental results [method (1) and method (2)], we show the values of γ used in method (2). Figure 7(a) shows the values of γ averaged from $t = 10$ s to 30 s for the heating-laser power $P = 78.7$ mW (circle), 46.7 mW (square), and 30.2 mW (triangle) as a function of the scanning radius R. The filled symbols indicate the results of the carboxylate-modified target particles and the empty symbols those of the amine-modified target particles. Although this is qualitative, we see that γ tends to decrease as R, i.e., the magnitude of the thermally induced flow decreases. Moreover, a comparison of different laser powers P shows that γ decreases with P. The cases of the amine-modified target produce significantly smaller γ than those of the carboxylate-modified target. These values of γ can be converted into K through Eqs. (8b) and (6); the results are summarized in Fig. 7(b). For the case of the carboxylate-modified surface, K seems to take a value around -0.4 μm^2 s^{-1} K^{-1}, while that of the amine-modified surface results in $K \approx -0.2$ μm^2 s^{-1} K^{-1}.

Finally, in Table I, we summarize the results of K obtained by the theoretical prediction [Eqs. (10) and (11)] and the experimental results [method (1) and method (2)], where the average over different values of R is taken for method (2) [see Fig. 7(b)]. Furthermore, Table II shows

TABLE I. The slip coefficient K (μm^2 s^{-1} K^{-1}) obtained from the model in Eqs. (10) and (11), based on Refs. [1,13], and the present experimental results using methods (1) and (2).

	Eq. (10)	Eq. (11)	Method (1)	Method (2)		
	Ref. [13]	Ref. [1]		$P = 78.7$ mW	$P = 46.7$ mW	$P = 30.2$ mW
Carboxylate-modified ($\zeta = -46.0$ mV)	-2.36	-0.94	-0.58 ± 0.20	-0.50 ± 0.02	-0.44 ± 0.02	-0.45 ± 0.03
Amine-modified ($\zeta = -23.7$ mV)	-0.58	-0.23	-0.34 ± 0.10	-0.25 ± 0.01		

TABLE II.　The slip coefficient $K = -\chi/T_f$ ($\mu m^2 \, s^{-1} \, K^{-1}$) reported in Ref. [1] for a glass substrate with or without a nonionic copolymer surfactant (Pluronic F-127) coating and Ref. [10] for a thin gold film on a glass substrate. In the references, the thermo-osmotic coefficient χ is reported and the values shown in this table are obtained for $T_f = 300$ K and 330 K.

Wall condition (experiments)	χ ($m^2 \, s^{-1}$)	K at $T_f = 300$ K	K at $T_f = 330$ K
Glass coated with Pluronic F-127 [1]	13×10^{-10}	-4.3	-3.9
Bare glass [1]	1.8×10^{-10}	-0.6	-0.5
Gold thin film on a glass substrate [10]	10×10^{-10}	-3.3	-3.0

the values of K computed from the existing experimental results of thermo-osmotic flows [1,10] with different surface details. All the values of K in both tables are negative, i.e., the flow is induced from the cold to the hot side. The magnitude of K in Table I has the same order $O(1)$ $\mu m^2 \, s^{-1} \, K^{-1}$ but quantitative agreement is not obtained between theory and experiment. However, methods (1) and (2) show similar values of K and capture the impact due to the surface modification predicted by Eqs. (10) and (11): K for the carboxylate-modified case is larger than that for the amine-modified case. Comparing Tables I and II, it can be seen that the slip coefficients obtained in the present experiments are close to that for bare glass.

The thermo-osmotic coefficients have also been computed using molecular dynamics simulations in Refs. [2,57] for a Lennard-Jones–type liquid-solid system and in Refs. [2,58–60] for water. The results were $\chi \sim O(10^{-8})$ $m^2 \, s^{-1}$ and one or two orders of magnitude greater than theory and experiment.

The reason for the quantitative discrepancy between theory and experiment cannot be fully clarified at the moment but let us point out some possibilities. First, Eq. (10) was derived under the thin-EDL and Debye-Hückel approximation. The former is valid because we use an electrolyte solution with a 10-mM ionic concentration. In fact, the computation of the Debye length λ of a monovalent electrolyte solution with 10 mM at room temperature gives $\lambda \approx 3$ nm, which is much smaller than the diameter 7 μm of the target particle. However, the latter approximation may be violated due to the non-negligible magnitude of the zeta potential compared with $k_B T_f$. Experiments, i.e., method (1) or method (2), may underestimate v_T^{target} or K because the target particle stays close to the microchannel walls due to a technical limitation in the experiment. Further improvement of the proposed method and its application to other systems is a future work.

V. CONCLUSIONS

In this paper, we propose an experimental method to characterize thermo-osmotic slip flows around a microparticle. The method utilizes the optical trapping of tracers around a microparticle, which indicates the generation of thermally induced flows near the particle surface through the change in the spatial distribution of the tracer. We apply the proposed method to the flow characterization around a microparticle under a strong temperature gradient created by the optical heating of a water solution.

The slip coefficient is estimated experimentally by using two methods: a thermophoretic velocity measurement of a target particle [method (1)] and a thermo-osmotic flow measurement around a target particle [method (2)], where the two methods are related through a simple physical model assuming a thermally induced slip boundary condition. The values of the slip coefficients obtained by the two methods are in reasonable agreement; i.e., we demonstrate that a flow is indeed induced along the surface of the particle under the temperature gradient and the agreement provides evidence that the flow is the major driving mechanism of thermophoresis. Furthermore, the experiments capture the difference in the surface modification predicted by the theory of a charged surface [13] with temperature variation.

The use of optical trapping of tracers, as demonstrated in the present paper, can also be applied to other flows near heated surfaces, such as those along the surface of heated Janus particles [41] and active composite particles [29] and heated Au films [10]. These thermally induced flows have possible applications on the conversion from heat to fluid motion. It has been proposed in Ref. [61] using numerical simulation that thermo-osmosis around fixed asymmetric objects under temperature gradient can be used as a fluidic pump, following the similar concept of the so-called Knudsen pump for the case of gases [62]. The flow measurement of thermally induced flows is necessary to explore such a system in detail.

The range of applications of the optical trapping of tracers proposed in this paper is not limited to thermally induced flows but also includes other microflows near surfaces: electro-osmosis [54], flows induced by engineered microswimmers [63], flows around active droplets driven by the interfacial-surface-tension gradient [64], and flows driven by living microorganisms [65,66]. Investigations of not only integrated quantities such as the flow rate in a channel or the motion of (and thus the force acting on) active matter but also the local flow near boundaries will explore a further understanding of nanofluidics, in which

surface effects are particularly significant, and their novel applications.

APPENDIX A: EXPERIMENTAL DETAILS

1. Overview

A schematic of the experiment is shown in Fig. 8. A microfluidics device made of a PDMS block and a cover glass is mounted on an inverted microscope (IX73, Olympus). The microchannel fabrication process has been given in Ref. [32]. The straight microchannel has a rectangular cross section with a height of $H = 17$ µm in the z direction, a width of 400 µm in the x direction, and a length > 3 mm in the y direction (see also Fig. 1). The height $H = 17$ µm is small enough to suppress the effect of thermal convection.

Two lasers with wavelengths of 1064 nm (Powerwave 1064, NPI lasers) and 1480 nm (FOL1439R50-667-1480, Furukawa Electric) are irradiated to the microchannel through an objective (×50, numerical aperture (NA) = 0.65; LCPLN50xIR, Olympus); the former (latter) is called a trapping (heating) laser in this paper. The trapping laser

is scanned in the focal plane by using a two-axis acousto-optic deflector (AOD; DTD-274HD6M & DE-272M, Intra Action) and captures tracers for flow visualization. The heating laser creates an inhomogeneous temperature field by using a photothermal effect of a water solution. Note that the absorption coefficient β of water at the wavelength of 1480 nm is $\beta = 2.4 \times 10^3$ m^{-1} [47,48]. This value of β is large enough for the necessary temperature elevation with a moderate laser power < 100 mW.

A background fluid flow in the microchannel in the y direction is controlled by adjusting the pressure difference ΔP between the inlet and outlet reservoirs (Fig. 8). To be more specific, ΔP is controlled with a resolution of 0.01 Pa by the water-level difference Δh between the two reservoirs, using a z stage. Before every experimental run, we confirm that the background fluid flow is absent. After an experiment, a nonuniform tracer distribution arises. Therefore, we induce a background flow to supply a fresh solution with a uniform tracer distribution to the test section.

Any residue bubbles in the microchannel, connecting tubes, and/or reservoirs can lead to loss of reproducibility of the experiments. To be more precise, if there are any residue bubbles, (a) the background flow never stops and there is always a very slow flow (< 1 µm) that can hinder the observation of thermally induced flows and (b) undesired and uncontrollable tracer motion occurs just after an onset of the heating-laser irradiation. Therefore, we pay special attention to the removal of bubbles. More specifically, before mounting the microfluidic device on
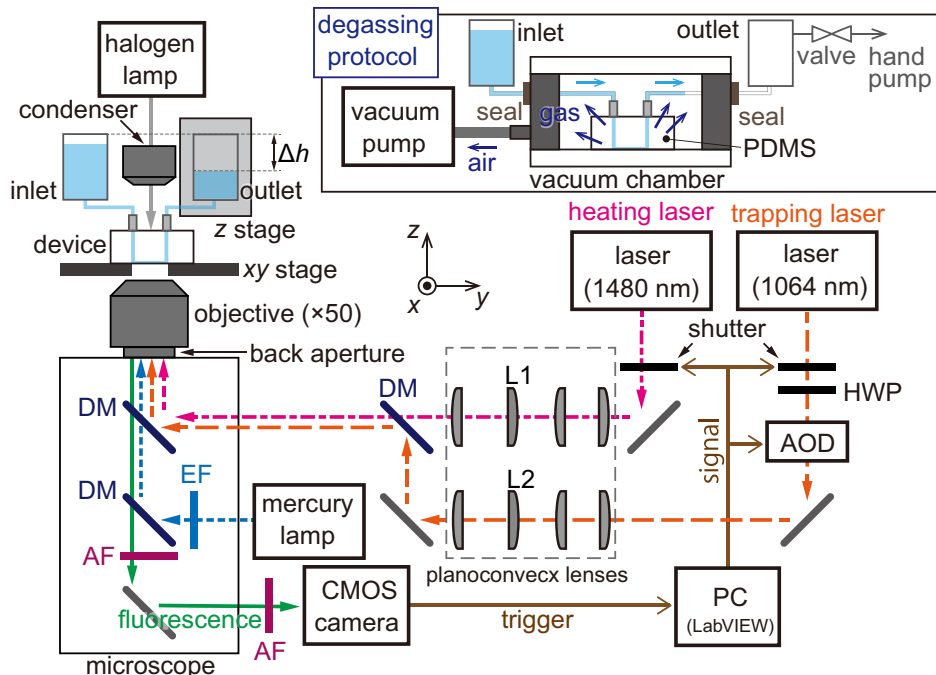

FIG. 8. An overview of the experimental setup. AF, absorption filters; AOD, acousto-optic deflector; DM, dichroic mirrors; EF, excitation filter; HWP, half-wave plate. The inset shows the degassing protocol.

the microscope, the entire device is degassed by placing only the PDMS-glass part in a vacuum chamber, as shown in the inset of Fig. 8. Since PDMS can absorb a gas [67], the degassing can avoid bubble formation and can also remove the residue bubble in the microchannel. By further degassing the empty outlet (see the inset of Fig. 8) using a hand pump, we can successfully fill the whole channel (including the tubes) with a sample solution without residue bubbles.

2. Sample solution

The target particles are nonfluorescent polystyrene spheres with a diameter of 7 μm and with carboxylate (01-02-703, Micromod) or amine (01-01-703, Micromod) surface modification. The tracer particles are fluorescent polystyrene spheres with yellow-green fluorescence (F8813, Molecular Probes) and have a diameter of 500 nm and a carboxylate surface modification. These as-purchased particles are dispersed in a tris(hydroxymethyl)amino-methane hydrochloride (tris-HCl) buffer solution (pH = 8.0, Nippon Gene) at a concentration of 10 mM. The concentrations of the target particles and tracers are 2.4×10^{-4} % and 4×10^{-2} %, respectively. The sample solution is sonicated for 5 min before use to avoid the agglomeration of tracers.

3. Optical setup

Two collimated lasers (for trapping and heating) are expanded using a set of planoconvex lenses, as shown in Fig. 8. A half-wave plate (HWP) is used for the optical path of the trapping laser to adjust the direction of linear polarization to that of the specification of the AOD. The lenses L1 and L2 and the AOD are placed at the conjugate planes of the back aperture of the objective lens, i.e., the motion of L1 and L2 perpendicular to the lenses and the beam deflection at the AOD can rotate the beam at the back aperture. In this way, we can move the laser focus in the focal plane in the x and y directions with minimal beam clipping [68].

A mercury lamp (U-HGLGPS, Olympus) with a band-pass filter (460–495 nm) is used as an excitation light source in the fluorescent imaging. A fluorescence from the tracers is collected by the same objective and is recorded by a scientific complementary metal-oxide semiconductor (sCMOS) camera (Zyla 5.5, Andor Technology), after removing undesired stray lights using absorption filters. The field depth in the z direction for this observation setup is 6 μm, as measured in our previous experiments with the same objective [51]. To observe the nonfluorescent target particle, we use a transmission light from a halogen lamp.

4. Experimental procedure

To immobilize the target particle on the upper surface in the microchannel, we use the trapping laser, following
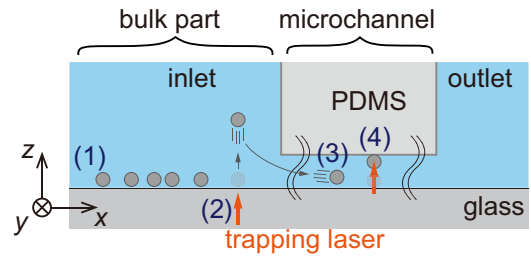

FIG. 9. A schematic of the immobilization process. (1) Many target particles are sedimented at the lower surface of the bulk part but (2) they are optically pushed by the laser with a wavelength of 1064 nm so that they disperse again. (3) The dispersed target particles are then driven into the microchannel. (4) The target particles are optically pushed to the ceiling of the microchannel until they stick there.

procedures (1)–(4) shown in Fig. 9. (1) The target particles have a non-negligible sedimentation speed. Thus, they tend to stay in the bulk part and they rarely come to the microchannel part. (2) We lift a target particle in the bulk by irradiating the trapping laser. (3) We induce a background flow to bring the target particle to the center of the microchannel part. (4) We again lift the target particle by irradiating the trapping laser and pushing it in the positive z direction to the upper surface of the microchannel, waiting about 10 min until the target particle sticks to the upper surface.

Note that the y position of the immobilized particle should be at about the center of the microchannel. Otherwise, we observe very slight but non-negligible tracer motion in the y direction just after the initiation of laser heating. We consider that this unwanted tracer motion does not originate from the existence of the residue bubbles, because the magnitude is much weaker than that in the case with the residue bubbles. In Fig. 1(b), we take the y axis, i.e., the direction of the background flow, perpendicular to the line of $\theta = 0$ to ensure that the accumulation (or depletion) of tracers (see Sec. IV) is not caused by such bias, if any.

After the immobilization of the target particle, we scan the trapping laser in a circular path with radius R with a power of 178 mW (after the objective). The scanning frequency is set to 200 Hz, which is high enough to avoid forcing tracers to orbit around the target particle. After a homogeneous distribution of tracers with respect to θ is realized, the heating laser with a power of P (after the objective) is irradiated, where $P = 13.5$, 30.2, 46.7, and 78.7 mW are used in this paper. The motion of the tracers is recorded with a frame rate of 20 frames/s for > 25 s.

APPENDIX B: TEMPERATURE PROFILE

We visualize the temperature profile of the sample solution in the x-y plane using a laser-induced
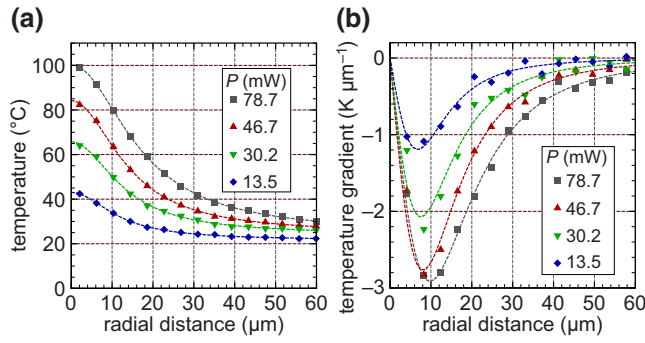
(a)

(b)

FIG. 10. (a) The temperature of a fluid and (b) a radial temperature gradient as a function of the radial distance r' from a heating spot [see Fig. 1(c)]. The power P of the laser with a wavelength 1480 nm are set to $P = 78.7$, 46.7, 30.2, and 13.5 mW.

fluorescence method [47–49,51,69]. The measurement process is exactly the same as that used in Refs. [49,51] and the details are omitted here. Note that the measured temperature profile presented below is the temperature of the fluid integrated over the depth (i.e., the z) direction.

Figure 10(a) shows the result of the temperature measurement for the laser power P used in this paper. The experimental data are shown by symbols and we fit these plots using half Lorentzian curves, $T_0 + \Delta T/(1 + (r'/\sigma)^2)$, where ΔT is the temperature increase at the beam center, T_0 is the temperature at infinity, σ is the half width at the midheight value of the temperature profile, and r' is the distance from the heating spot. The parameters used in the fitting are summarized in Table III. The corresponding radial gradient is also shown in Fig. 10(b).

The magnitude of the temperature gradient is more than 2 K μm^{-1} around the target particle for $P = 78.7$ mW, which is placed at $r'(= L) \approx 18$ μm. This huge temperature gradient is required to observe the thermo-osmotic flow with a detectable magnitude. In some applications, one may need to suppress a laser power and/or the amount of heat generation. One feasible approach to observe the thermo-osmotic flow around a microparticle with a weaker laser power is to use an Au-coated Janus particle, as proposed in Ref. [41], in which the steep temperature gradient is generated directly on the particle surface using a laser power about 1 mW.

The model in Eq. (8b) assumes a linear temperature gradient of fluid far from the target particle. Here, this

assumption is discussed in detail. The temperature profile is computed by using the steady heat-conduction equation for the water solution together with PDMS (upper part) and the glass substrate (lower part), i.e., three layers with an axisymmetric laser heat source. Here, due to the negligible thermal Péclet number, we neglect the convection term in the water layer. The computational model is similar to that used in Ref. [70] and therefore we omit the details here and we only summarize the physical parameters used in the computation: the thermal conductivities of water, PDMS, and the (borosilicate) glass are 0.6, 0.15, and 1.4 W K^{-1} m^{-1}, respectively; the heights of the water, PDMS, and glass layers are 17, 500, and 100 μm, respectively; the ambient temperatures at the outer surfaces of the PDMS and glass are fixed to 24°C; the absorption coefficient of the water is 2.4×10^3 m^{-1}; and the laser is a loosely focused Gaussian beam with a beam waist of 12 μm at the focal plane $z = 17$ μm. The laser power is $P = 86$ mW.

The resulting axisymmetric temperature profile is plotted in Fig. 11. Figure 11(a) shows the temperature contours in the r'-z plane, where r' is the distance from the beam axis, and the dashed circle indicates the position of the target particle. (Note that this computation does not take into account the presence of the particle.) Figure 11(b) is the radial temperature profile for various heights $z = 10.5, \ldots,$ 17 μm. The experimental result (which is an average in the z direction) with $P = 46.7$ mW is also plotted. The

(a)

(b)
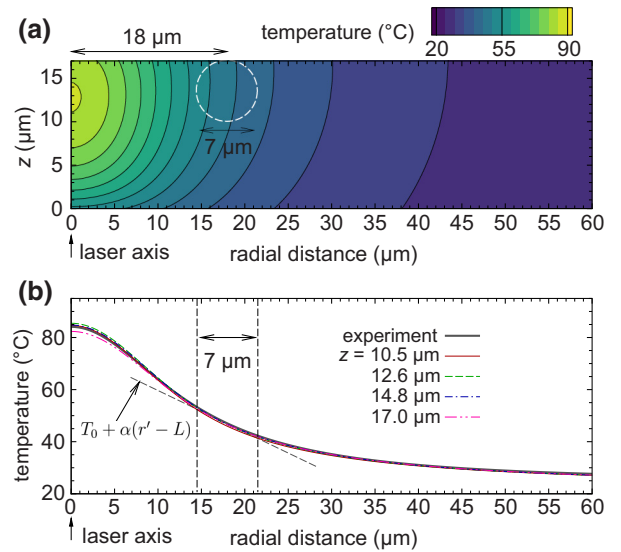
FIG. 11. The temperature profile obtained by the heat-conduction equations for three-layer systems of water, PDMS, and glass. (a) The temperature contours in the r'-z plane. (b) The radial temperature profile for $z = 10.5$, 12.6, 14.8, and 17.0 μm. The experimental result with $P = 46.7$ mW is also plotted. The dashed line is a linear function $T_0 + \alpha(r' - L)$ with $T_0 = 320$ K, $\alpha = -1.6$ K μm^{-1}, and $L = 18$ μm with respect to the radial distance r'.

TABLE III. The parameters used in the fitting of Fig. 10.

P (mW)	ΔT (K)	σ (μm)	T_0 (K)
78.7	75.7	16.9	24.6
46.7	59.5	14.0	24.6
30.2	41.6	13.1	24.1
13.5	21.4	11.7	21.6

computation somehow underestimates the experimental results; however, the spatial profiles between experiment and computation agree very well. First, we note from the figure that the water temperature is almost uniform in the z direction in the range 10 μm $< z <$ 17 μm, which covers the vertical position of the target particle. This is due to the low thermal conductivity of the PDMS consisting of the upper wall. Thus, we may roughly consider that the temperature around the target particle is independent of z.

As shown in Fig. 11(b), the temperature profile is approximated by a half Lorentzian curve and not a unidirectional linear function. Therefore, the assumption of the model in Sec. III, i.e., a unidirectional linear temperature profile far from the particle, is not fully satisfied here. Nevertheless, we expect the assumption not to result in qualitative differences and we prioritize the simplicity of the model to obtain the analytical expression [Eq. (8b)] to be compared with the experimental data.

APPENDIX C: VALIDITY OF THE MODEL

In this appendix, we discuss the adequateness of the model given in Eq. (8b) by observing the temperature-gradient (i.e., α) dependence. The parameter γ is expected to be linear in the temperature gradient α in our model [see Eq. (8b) together with Eq. (6)]. Considering that the laser power P affects not only the temperature gradient α but also the temperature T_f (see Fig. 10) and also that the diffusion coefficient D depends on T_f, we investigate whether $v^*|_{r=R} = \gamma(D/R)$ is linear with respect to α (i.e., for different P and fixed R), rather than γ itself. To observe this trend, we show in Table IV the values of $\gamma(D/R)/\alpha$, together with other experimental parameters. For each R, we consider that $\gamma(D/R)/\alpha$ takes similar values and this trend indicates that $\gamma(D/R)$ is close to a linear function of α. The deviation from the linear function may be due

to some nonlinearity and/or the limitations of the present physical model.

APPENDIX D: DATA-ANALYSIS PROCEDURE

Let f_{ij}^n be the intensity of an obtained image, where the indices i and j are the pixel numbers in the x and y directions and n is the frame number. First, we average the images over n_0 frames with $n_0 = 100$ (over 5 s) to reduce noise and define them as $\bar{f}_{ij}^n = (1/n_0) \sum_{m=n-n_0+1}^{n} f_{ij}^m$. Then, we subtract the background value, which is the minimum value over the whole pixel of $\bar{f}_{ij}^n$. The θ direction is divided into intervals and we introduce $\theta_p = p\Delta\theta$ ($p = -p_0, \ldots, p_0$) with $p_0 = 10$ and $\Delta\theta = \pi/p_0$. To analyze the result with $r = R$, we average the intensity $\bar{f}_{ij}^n$ over a domain $(r, \theta) \in [R - \Delta r, R + \Delta r] \times [\theta_p, \theta_p + \Delta\theta]$ with $\Delta r \approx 258$ nm. This averaged value is denoted by F_p^n and we then compute the spatial average over the whole range of θ values, i.e., $\bar{F}^n = (1/2\pi) \sum_{\text{all } p} F_p^n \Delta\theta$. The results shown in the main text (e.g., Sec. IV B) are the relative intensity, namely, $F_p^n/\bar{F}^n$ [$=$ (intensity near $\theta = \theta_p$)/(intensity averaged over the whole range of θ values)].

Next, we describe details of the fitting procedure. In practice, the value of the normalization constant c_0 in Eq. (8) is not free for us to choose but should be determined in the following manner. We fit the experimental data (i.e., the relative intensity explained above) using the function $c_{\text{fit}} = c_0 \exp(\gamma \cos(\theta - \theta')) + c'$ to obtain γ, where θ' and c' are auxiliary fitting parameters to absorb the unavoidable shifts in the experimental results. Here, c_0 is determined so that $\int_{-\pi}^{\pi} c_{\text{fit}} d\theta = 1$, because the experimental data are normalized by the average over the whole range of θ values as described above. Thus, c_0 is a function of γ and c'. By noting the identity $\int_{-\pi}^{\pi} \exp(\gamma \cos \theta) d\theta = 2\pi \mathcal{I}_0(\gamma)$, where $\mathcal{I}_0$ is the modified Bessel function of the first kind, we obtain $c_0 = (1 - 2\pi c')/(2\pi \mathcal{I}_0(\gamma))$. The function $\mathcal{I}_0$ can

TABLE IV. The values of $\gamma(D/R)/\alpha$ for various experimental conditions. T_f and α are obtained from Fig. 10 at the position $r' = 18$ μm. The value of $D = k_B T_f/(3\pi d^{\text{tracer}}\eta)$ is obtained from the Stokes-Einstein relation, where k_B is the Boltzmann constant, d^{tracer} is the diameter of the tracers, and η is the temperature-dependent viscosity [55].

R (μm)	P (mW)	T_f (K)	α (K μm^{-1})	D (μm^2 s^{-1})	γ	$\gamma(D/R)/\alpha$ (μm^2 s^{-1} K^{-1})
4.4	78.7	333	-2.10	2.07	1.18	2.65×10^{-1}
	46.7	320	-1.60	1.61	0.93	2.14×10^{-1}
	30.2	312	-1.00	1.35	0.64	1.99×10^{-1}
5.4	78.7	333	-2.10	2.07	1.03	1.89×10^{-1}
	46.7	320	-1.60	1.61	0.87	1.62×10^{-1}
	30.2	312	-1.00	1.35	0.52	1.32×10^{-1}
6.5	78.7	333	-2.10	2.07	0.90	1.37×10^{-1}
	46.7	320	-1.60	1.61	0.61	0.95×10^{-1}
	30.2	312	-1.00	1.35	0.59	1.23×10^{-1}
7.5	78.7	333	-2.10	2.07	0.58	0.77×10^{-1}
	46.7	320	-1.60	1.61	0.39	0.53×10^{-1}
	30.2	312	-1.00	1.35	0.37	0.69×10^{-1}

TABLE V. The coefficient of determination R^2 for the fitting procedure used in the present paper. For typical examples of the actual fitting curves, see Figs. 4, 5, and 6. For the actual fitting values, see Fig. 7(a).

R (μm)	Carboxylate-modified			Amine-modified	No target particle
	$P = 78.7$ mW	$P = 46.7$ mW	$P = 30.2$ mW	$P = 78.7$ mW	$P = 78.7$ mW
4.4	0.97	0.98	0.97	0.61	0.73
5.4	0.97	0.98	0.85	0.25	—
6.5	0.94	0.92	0.84	0.01	—
7.5	0.86	0.69	0.66	0.01	—

be approximated by an elementary function [71], which is used in the actual fit. The procedure described above is carried out using the ImageJ software.

The adequateness of the fitting is evaluated by the coefficient of determination R^2, where $R^2 (< 1)$ close to unity indicates a successful fitting. The values of R^2 for the fitting procedure are summarized in Table V. For the cases with the carboxylate-modified target particles, the signal-to-noise ratio is good and the model given in Eq. (8) fits the experimental data well, i.e., $R^2 \approx 1$. For the cases with the amine-modified target and the case without the target particle, the value of R^2 is decreased to > 0.6 for $P = 78.7$ mW, but the model in Eq. (8) can still be considered to fit the experimental data. In the analysis of the present paper, the data with bad values of $R^2 < 0.6$ due to stochastic noise are not used in the case without the target particle.

[1] A. P. Bregulla, A. Würger, K. Günther, M. Mertig, and F. Cichos, Thermo-osmotic flow in thin films, Phys. Rev. Lett. **116**, 188303 (2016).

[2] L. Fu, S. Merabia, and L. Joly, What controls thermo-osmosis? Molecular simulations show the critical role of interfacial hydrodynamics, Phys. Rev. Lett. **119**, 214501 (2017).

[3] K. Proesmans and D. Frenkel, Comparing theory and simulation for thermo-osmosis, J. Chem. Phys. **151**, 124109 (2019).

[4] P. Anzini, G. M. Colombo, Z. Filiberti, and A. Parola, Thermal forces from a microscopic perspective, Phys. Rev. Lett. **123**, 028002 (2019).

[5] P. Anzini, Z. Filiberti, and A. Parola, Fluid flow at interfaces driven by thermal gradients, Phys. Rev. E **106**, 024116 (2022).

[6] S. M. Mousavi, I. Kasianiuk, D. Kasyanyuk, S. K. P. Velu, A. Callegari, L. Biancofiore, and G. Volpe, Clustering of Janus particles in optical potential driven by hydrodynamic fluxes, Soft Matter **15**, 5748 (2019).

[7] M. Trivedi, D. Saxena, W. K. Ng, R. Sapienza, and G. Volpe, Self-organized lasers from reconfigurable colloidal assemblies, Nat. Phys. **18**, 939 (2022).

[8] H. Xu, X. Zheng, and X. Shi, Surface hydrophilicity-mediated migration of nano/microparticles under temperature gradient in a confined space, J. Colloid Interface Sci. **637**, 489 (2023).

[9] X. Lou, N. Yu, R. Liu, K. Chen, and M. Yang, Dynamics of a colloidal particle near a thermoosmotic wall under illumination, Soft Matter **14**, 1319 (2018).

[10] M. Fränzl and F. Cichos, Hydrodynamic manipulation of nano-objects by optically induced thermo-osmotic flows, Nat. Commun. **13**, 656 (2022).

[11] B. V. Derjaguin, N. V. Churaev, and M. M. Muller, *Surface Forces* (Springer, New York, 1987).

[12] J. L. Anderson, Colloid transport by interfacial forces, Annu. Rev. Fluid Mech. **21**, 61 (1989).

[13] S. Fayolle, T. Bickel, and A. Würger, Thermophoresis of charged colloidal particles, Phys. Rev. E **77**, 041404 (2008).

[14] S. N. Rasuli and R. Golestanian, Soret motion of a charged spherical colloid, Phys. Rev. Lett. **101**, 108301 (2008).

[15] A. Würger, Transport in charged colloids driven by thermoelectricity, Phys. Rev. Lett. **101**, 108302 (2008).

[16] E. Ruckenstein, Can phoretic motions be treated as interfacial tension gradient driven phenomena?, J. Colloid Interface Sci. **83**, 77 (1981).

[17] A. Würger, Thermophoresis in colloidal suspensions driven by Marangoni forces, Phys. Rev. Lett. **98**, 138301 (2007).

[18] Y. Kim, H. Ding, and Y. Zheng, Investigating water/oil interfaces with opto-thermophoresis, Nat. Commun. **13**, 3742 (2022).

[19] G. Baffou, *Thermoplasmonics* (Cambridge University Press, Cambridge, 2017).

[20] G. Baffou, F. Cichos, and R. Quidant, Applications and challenges of thermoplasmonics, Nat. Mater. **19**, 946 (2020).

[21] D. G. Kotsifaki and S. N. Chormaic, The role of temperature-induced effects generated by plasmonic nanostructures on particle delivery and manipulation: A review, Nanophotonics **11**, 2199 (2022).

[22] R. Piazza and A. Parola, Thermophoresis in colloidal suspensions, J. Phys.: Condens. Matter **20**, 153102 (2008).

[23] R. Piazza, Thermophoresis: Moving particles with thermal gradients, Soft Matter **4**, 1740 (2008).

[24] A. Würger, Thermal non-equilibrium transport in colloids, Rep. Prog. Phys. **73**, 126601 (2010).

[25] T. Tsuji, K. Kozai, H. Ishino, and S. Kawano, Direct observations of thermophoresis in microfluidic systems, Micro Nano Lett. **12**, 520 (2017).

[26] H.-R. Jiang, N. Yoshinaga, and M. Sano, Active motion of a Janus particle by self-thermophoresis in a defocused laser beam, Phys. Rev. Lett. **105**, 268302 (2010).

[27] T. Bickel, A. Majee, and A. Würger, Flow pattern in the vicinity of self-propelling hot Janus particles, Phys. Rev. E **88**, 012301 (2013).

[28] S. Auschra, A. Bregulla, K. Kroy, and F. Cichos, Thermo-taxis of Janus particles, Eur. Phys. J. **44,** 90 (2021).

[29] D. Paul, R. Chand, and G. V. P. Kumar, Optothermal evolution of active colloidal matter in a defocused laser trap, ACS Photonics **9,** 3440 (2022).

[30] D. Vigolo, R. Rusconi, H. A. Stone, and R. Piazza, Thermophoresis: Microfluidics characterization and separation, Soft Matter **6,** 3489 (2010).

[31] Y. T. Maeda, A. Buguin, and A. Libchaber, Thermal separation: Interplay between the Soret effect and entropic force gradient, Phys. Rev. Lett. **107,** 038301 (2011).

[32] T. Tsuji, S. Saita, and S. Kawano, Dynamic pattern formation of microparticles in a uniform flow by an on-chip thermophoretic separation device, Phys. Rev. Appl. **9,** 024035 (2018).

[33] A. Sanjuan, A. Errarte, and M. M. Bou-Ali, Analysis of thermophoresis for separation of polystyrene microparticles in microfluidic devices, Int. J. Heat Mass Transfer **189,** 122690 (2022).

[34] C. J. Wienken, P. Baaske, U. Rothbauer, D. Braun, and S. Duhr, Protein-binding assays in biological liquids using microscale thermophoresis, Nat. Commun. **1,** 100 (2010).

[35] S. A. I. Seidel, C. J. Wienken, S. Geissler, M. Jerabek-Willemsen, S. Duhr, A. Reiter, D. Trauner, D. Braun, and P. Baaske, Label-free microscale thermophoresis discriminates sites and affinity of protein-ligand binding, Angew. Chem., Int. Ed. **51,** 10656 (2012).

[36] C. Liu, J. Zhao, F. Tian, L. Cai, W. Zhang, Q. Feng, J. Chang, F. Wan, Y. Yang, B. Dai, Y. Cong, B. Ding, J. Sun, and W. Tan, Low-cost thermophoretic profiling of extracellular-vesicle surface proteins for the early detection and classification of cancers, Nat. Biomed. Eng. **3,** 183 (2019).

[37] L. Lin, M. Wang, X. Peng, E. N. Lissek, Z. Mao, L. Scarabelli, E. Adkins, S. Coskun, H. E. Unalan, B. A. Korgel, L. M. Liz-Marzán, E.-L. Florin, and Y. Zheng, Opto-thermoelectric nanotweezers, Nat. Photonics **12,** 195 (2018).

[38] K. Setoura, T. Tsuji, S. Ito, S. Kawano, and H. Miyasaka, Opto-thermophoretic separation and trapping of plasmonic nanoparticles, Nanoscale **11,** 21093 (2019).

[39] L. Lin, X. Peng, X. Wei, Z. Mao, C. Xie, and Y. Zheng, Thermophoretic tweezers for low-power and versatile manipulation of biological cells, ACS Nano **11,** 3147 (2017).

[40] F. M. Weinert and D. Braun, Observation of slip flow in thermophoresis, Phys. Rev. Lett. **101,** 168301 (2008).

[41] A. P. Bregulla and F. Cichos, Flow fields around pinned self-thermophoretic microswimmers under confinement, J. Chem. Phys. **151,** 044706 (2019).

[42] A. Ashkin and J. M. Dziedzic, Optical levitation by radiation pressure, Appl. Phys. Lett. **19,** 283 (1971).

[43] A. Ashkin, J. M. Dziedzic, J. E. Bjorkholm, and S. Chu, Observation of a single-beam gradient force optical trap for dielectric particles, Opt. Lett. **11,** 288 (1986).

[44] T. Tsuji, K. Doi, and S. Kawano, Optical trapping in micro- and nanoconfinement systems: Role of thermo-fluid dynamics and applications, J. Photochem. Photobiol. C: Photochem. Rev., 100533 (2022).

[45] G. Volpe, O. M. Maragò, H. Rubinsztein-Dunlop, G. Pesce, A. B. Stilgoe, G. Volpe, G. Tkachenko, V. G. Truong, S. N. Chormaic, F. Kalantarifard et al., Roadmap for optical tweezers, J. Phys.: Photonics **5,** 022501 (2023).

[46] S. Duhr and D. Braun, Why molecules move along a temperature gradient, Proc. Natl. Acad. Sci. **103,** 19678 (2006).

[47] M. L. Cordero, E. Verneuil, F. Gallaire, and C. N. Baroud, Time-resolved temperature rise in a thin liquid film due to laser absorption, Phys. Rev. E **79,** 011201 (2009).

[48] D. Rivière, B. Selva, H. Chraibi, U. Delabre, and J.-P. Delville, Convection flows driven by laser heating of a liquid layer, Phys. Rev. E **93,** 023112 (2016).

[49] T. Tsuji, Y. Sasai, and S. Kawano, Thermophoretic manipulation of micro- and nanoparticle flow through a sudden contraction in a microchannel with near-infrared laser irradiation, Phys. Rev. Appl. **10,** 044005 (2018).

[50] Y. Sone, Molecular Gas Dynamics: Theory, Techniques, and Applications (Birkhäuser, Boston, 2007).

[51] T. Tsuji, S. Taguchi, and H. Takamatsu, Switching between laser-induced thermophoresis and thermal convection of liquid suspension in a microgap with variable dimension, Electrophoresis **42,** 2401 (2021).

[52] S. Duhr and D. Braun, Two-dimensional colloidal crystals formed by thermophoresis and convection, Appl. Phys. Lett. **86,** 131921 (2005).

[53] D. B. Mayer, T. Franosch, C. Mast, and D. Braun, Thermophoresis beyond local thermodynamic equilibrium, Phys. Rev. Lett. **130,** 168202 (2023).

[54] X. Xuan, B. Xu, D. Sinton, and D. Li, Electroosmotic flow with Joule heating effects, Lab Chip **4,** 230 (2004).

[55] J. H. Knox and K. A. McCormack, Temperature effects in capillary electrophoresis. 1: Internal capillary temperature and effect upon performance, Chromatographia **38,** 207 (1994).

[56] B. V. Derjaguin and Y. Yalamov, Theory of thermophoresis of large aerosol particles, J. Colloid Sci. **20,** 555 (1965).

[57] R. Ganti, Y. Liu, and D. Frenkel, Molecular simulation of thermo-osmotic slip, Phys. Rev. Lett. **119,** 038002 (2017).

[58] W. Q. Chen, M. Sedighi, and A. P. Jivkov, Thermo-osmosis in hydrophilic nanochannels: Mechanism and size effect, Nanoscale **13,** 1696 (2021).

[59] C. Herrero, M. D. S. Féliciano, S. Merabia, and L. Joly, Fast and versatile thermo-osmotic flows with a pinch of salt, Nanoscale **14,** 626 (2022).

[60] M. Ouadfel, M. D. S. Féliciano, C. Herrero, S. Merabia, and L. Joly, Complex coupling between surface charge and thermo-osmotic phenomena, Phys. Chem. Chem. Phys. **25,** 24321 (2023).

[61] Z. Tan, M. Yang, and M. Ripoll, Microfluidic pump driven by anisotropic phoresis, Phys. Rev. Appl. **11,** 054004 (2019).

[62] X. Wang, T. Su, W. Zhang, Z. Zhang, and S. Zhang, Knudsen pumps: A review, Microsyst. Nanoeng. **6,** 26 (2020).

[63] M. Pal, I. Fouxon, A. M. Leshansky, and A. Ghosh, Fluid flow induced by helical microswimmers in bulk and near walls, Phys. Rev. Res. **4,** 033069 (2022).

[64] C. Jin, Y. Chen, C. C. Maass, and A. J. Mathijssen, Collective entrainment and confinement amplify transport by

schooling microswimmers, Phys. Rev. Lett. **127**, 088006 (2021).

[65] K. Drescher, R. E. Goldstein, N. Michel, M. Polin, and I. Tuval, Direct measurement of the flow field around swimming microorganisms, Phys. Rev. Lett. **105**, 168101 (2010).

[66] R. E. Goldstein, Green algae as model organisms for biological fluid dynamics, Annu. Rev. Fluid Mech. **47**, 343 (2015).

[67] K. Hosokawa, K. Sato, N. Ichikawa, and M. Maeda, Power-free poly (dimethylsiloxane) microfluidic devices for gold nanoparticle-based DNA analysis, Lab Chip **4**, 181 (2004).

[68] K. C. Neuman and S. M. Block, Optical trapping, Rev. Sci. Instrum. **75**, 2787 (2004).

[69] D. Braun and A. Libchaber, Trapping of DNA by thermophoretic depletion and convection, Phys. Rev. Lett. **89**, 188103 (2002).

[70] C. Hosokawa, T. Tsuji, T. Kishimoto, T. Okubo, S. N. Kudoh, and S. Kawano, Convection dynamics forced by optical trapping with a focused laser beam, J. Phys. Chem. C **124**, 8323 (2020).

[71] J. Olivares, P. Martin, and E. Valero, A simple approximation for the modified Bessel function of zero order $I_0(x)$, J. Phys.: Conf. Ser. **1043**, 012003 (2018).